China Instrument and Control Society
Instrumentation
INSTRUMENTATION, Vol. 13, No. 3, 2026
https://doi.org/10.15878/j.instr.202600421

Article

Volume Measurement of Lunar Soil in the Chang'E-6 Sampling Container Using a Single Camera

Jiaqi Liang[1,†], Ming Yang[1,†], Yanhong Zheng[2], Lvting Meng[2], Xiangjin Deng[2,*], Yufu Qu[1,*]

[1] School of Instrumentation and Optoelectronic Engineering, Beihang University, Beijing 100191, China

[2] Beijing Institute of Spacecraft System Engineering, China Academy of Space Technology, Beijing 100094, China

[*] Corresponding author email: qyf@buaa.edu.cn (Y. Qu); dengxiangjin@cast501.cn (X. Deng)

Abstract: The Chang'E-6 mission aims to return lunar soil samples from the farside of the Moon. To assist the mission in deciding the optimal time to stop scooping, a complete measurement method comprising an image acquisition scheme and a measurement algorithm is proposed to measure the volume of lunar soil in the container. A camera captures images at two different positions, which serve as the left and right views of a stereo pair. By capturing images with different exposure times, information in both the low-illumination and high-illumination regions is obtained. A multi-target template detection method is designed to avoid the erroneous target extraction caused by a fixed threshold, and the complex 3D point cloud extraction is avoided by detecting the lunar soil region in the image. Experiments in a lunar simulation environment on Earth demonstrate that the method measures the volume of lunar soil accurately, with an absolute error of at most 17 cm^3. On June 3, 2024, the volume of lunar soil measured after eight scoops on the Moon was 1393 cm^3. These measurements assisted the Chang'E-6 team in confirming that the lunar soil in the sampling container had met the established objectives and that it was the optimal time to stop scooping.

Keywords: Chang'E-6 mission; volume measurement of lunar soil; 3D vision; pose estimation; point cloud extraction

Copyright: © 2026 by the authors. This article is licensed under a Creative Commons Attribution 4.0 International License (CC BY) license (https://creativecommons.org/licenses/by/4.0/).

Citation: Liang J, Yang M, Zheng Y, Meng L, Deng X, Qu Y. Volume Measurement of Lunar Soil in the Chang'E-6 Sampling Container Using a Single Camera. Instrumentation, 2026, 13(3). https://doi.org/10.15878/j.instr.202600421

1 Introduction

As the closest natural satellite to Earth, the Moon has become the primary target of deep space exploration[1, 2]. From the late 1960s, humanity has conducted multiple explorations of the Moon, with lunar soil collection being one of the most important tasks. Through the study of collected lunar soil, scientists have revealed the properties of the Moon and the composition of lunar rocks, and inferred the Moon's origin and evolutionary history[3,4,5,6,7,8]. From the late 1960s to the mid-1980s, the United States collected 381.7 kg of lunar soil across six Apollo missions. The Soviet Union collected 335 g of lunar soil during three Luna missions. The Chang'E program in China regards lunar soil collection as one of its key objectives. After the last robotic sampling by Luna-24 in 1976, no large-scale lunar soil sampling missions were conducted until China's Chang'E-5 mission collected 1731 g of lunar soil from the Northern Oceanus Procellarum in 2020[1,9,10,11,12]. Following the success of the Chang'E-5 mission, Chang'E-6 is the first mission to return samples from the lunar farside; it represents the final stage of the three-phase Chinese Lunar Exploration Program (CLEP) and will significantly advance lunar exploration and research[13,14,15].

In the previous Chang'E-5 mission, the sample container was photographed with a camera mounted on the robotic arm, and the volume of lunar soil inside the

container was estimated by eye from the captured images. This approach has several drawbacks. As shown in Fig. 1, the depth of the container limits the light reaching its interior, so the images are dark and the soil volume is difficult to estimate visually. Moreover, an eye-based estimate is highly subjective, making it difficult for ground personnel to reach accurate and consistent decisions on whether to continue scooping. Considerable time is therefore spent discussing whether to continue, which is critical throughout the Chang'E-6 soil collection mission.

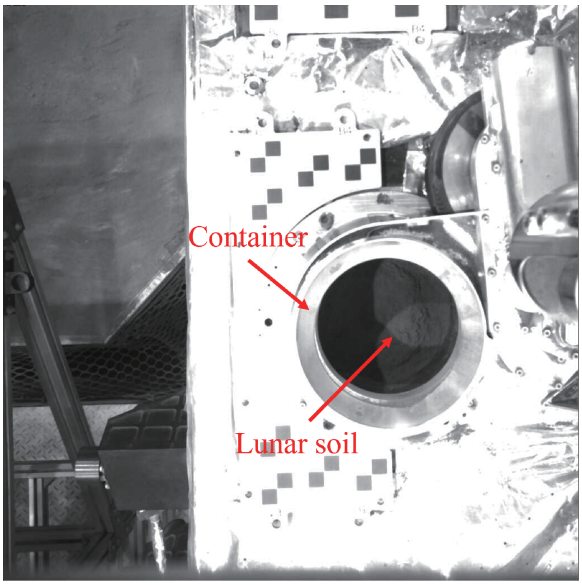


Fig.1 The container filled with lunar soil in a high-dynamic-range scene.

In lunar soil sampling missions, the soil is typically placed in containers or bags for return to Earth. During the Apollo missions, astronauts collected lunar soil with specialized tools and stored it in designated containers[9]. The Luna missions used a drilling sampler and a robotic scooping sampler, and the collected soil was stored in the soil container of the return apparatus before being brought back to Earth[11]. The Chang'E-5 mission used both scooping and drilling to collect lunar soil. The scooped soil was stored in a sampling container (referred to as the "container" hereafter) fixed to the lander, and this container was subsequently transferred to the returner for transport back to Earth[10]. The Chang'E-6 mission used the same equipment and collection method as Chang'E-5[16]. Given the tight schedule and the complexities of lunar farside sampling, a vision-based implementation for terrain analysis and sampler pose measurement was specifically developed to enhance efficiency and autonomy[17]. The container ultimately determines how much lunar soil can be brought back, so the collected amount must remain within an optimal range. Because lunar soil has high research value, as much soil as possible should be collected within the limited sampling time and container volume; however, collecting too much consumes additional sampling time and may prevent the container from being sealed properly. Measuring the volume of lunar soil in the container is therefore essential for determining the optimal time to stop collection.

Chang'E-6 requires an accurate estimate of the lunar soil volume inside the container[16]. Estimating this volume from 2D image information alone is difficult. However, with the advancement of deep learning, visual 3D algorithms can recover the 3D structure of the lunar soil inside the container from the captured images, and numerous methods can obtain 3D point clouds from images, providing substantial support for accurate volume measurement[18,19,20]. Recent deep-learning-based volumetric imaging networks further enable real-time, high-resolution three-dimensional reconstruction across scales, and non-contact optical elastography offers an additional imaging-based measurement route[21, 22]. Machine-vision-based volume measurement has therefore been widely applied across various industries. Existing vision-based volume measurement methods can be grouped by how they recover 3D geometry. Structure-from-Motion (SfM) photogrammetry reconstructs a scene from multiple overlapping views and has been used to measure the volume of undisturbed soil[23] and of wood from unmanned aerial vehicle (UAV) imagery[24]; smartphone-based SfM has also been compared against Terrestrial Laser Scanner (TLS) measurements to validate the accuracy of the reconstructed models[25]. Stereo and binocular reconstruction estimates depth from a pair of calibrated views and has been applied to the volume of contained soil without a pre-existing container model[26], to canopy volume for UAV-based chemical application[27], and to tree volume using a robot with two cameras placed at different positions[28]. A third group recovers volume from active depth sensing or from geometric priors: RGB-D and depth cameras have measured the volume of irregular objects[29] and of livestock[30, 31]; other approaches reconstruct volumetric displacement from 3D reconstruction[32], identify material piles within point clouds[33], or estimate the payload of construction-waste trucks from a monocular image and a known truck profile[34]. Despite this breadth, these approaches are largely demonstrated in well-lit terrestrial scenes and typically assume a known camera pose, multiple views, or an active depth sensor.

Vision-based volumetric measurement has been studied extensively in various fields, driven by advances such as ultrafast nano-spectroscopy, neural meta-imaging, and cross-scale volumetric imaging[21, 35, 36]. However, few studies have addressed volumetric measurement of target objects using vision technology in lunar exploration. Compared with measurement tasks in other fields, measuring the volume of lunar soil inside the Chang'E-6 container poses more stringent challenges and limitations, which we list as follows:

1. The measurement algorithm must be robust while minimizing manual intervention and complexity, thereby

saving time.

2. In terms of hardware, Chang'E-6 has only one movable camera to capture images of the container.

3. The brightness inside the sample container is low because only a limited amount of light enters it.

4. The deformation of the robotic arm cannot be ignored, making it impossible to obtain the camera pose directly.

To address these challenges, we designed a complete image acquisition scheme and measurement algorithm to automatically measure the volume of lunar soil in the sampling container under the constraints of the Chang'E-6 mission. Because only one camera is available, images were captured at two different positions to serve as the left and right views of a stereo pair. The exposure time was adjusted to acquire images with different brightness levels, so that the lunar soil surface inside the container and the target plate outside it could be extracted separately. To handle the non-negligible deformation of the robotic arm, a multi-target template matching algorithm was designed to extract all target points, after which the camera pose was estimated and stereo rectification was applied. The 3D point cloud of the entire scene was then reconstructed by stereo matching, and a simple yet reliable method was developed to extract the point cloud corresponding to the lunar soil. Finally, a reference plane was adaptively selected to divide the volume into two parts and compute the total volume. We built a lunar simulation environment with equipment identical to that used in the Chang'E-6 mission and evaluated the proposed algorithm in this environment. The results show that the method measures the lunar soil volume with high accuracy. During the Chang'E-6 mission, the method provided quantitative and qualitative measurements of the lunar soil volume, supporting the Chang'E-6 team in determining the amount of soil in the container and in deciding whether to continue collection, thereby saving considerable time.

2 Image Acquisition Hardware System and Scheme

Based on the hardware configuration and requirements of the Chang'E-6 mission, we design a tailored image acquisition scheme and the corresponding image processing algorithms for measuring the volume of lunar soil in the container.

Fig. 2 shows the image acquisition equipment for lunar soil volume measurement on Chang'E-6. Fig. 2(a) shows the lunar simulation environment constructed on Earth with equipment identical to that used in the mission, and Fig. 2(b) presents a simplified model of the hardware. A monocular camera is mounted at the end of a robotic arm, which allows the camera to move. However, due to non-negligible robotic arm deformation, the camera pose cannot be obtained directly from joint angles, and vision-based pose measurement has proven effective for such challenges in the Chang'E-6 mission[17]. The lunar soil is stored in the sampling container, around which a target plate is fixed. This plate contains eight targets with known three-dimensional coordinates, and the camera has adjustable exposure settings to adapt to the complex lighting conditions. Fig. 2(c) shows an example image captured by the system, which mainly contains the target plate and the container filled with a certain amount of soil.

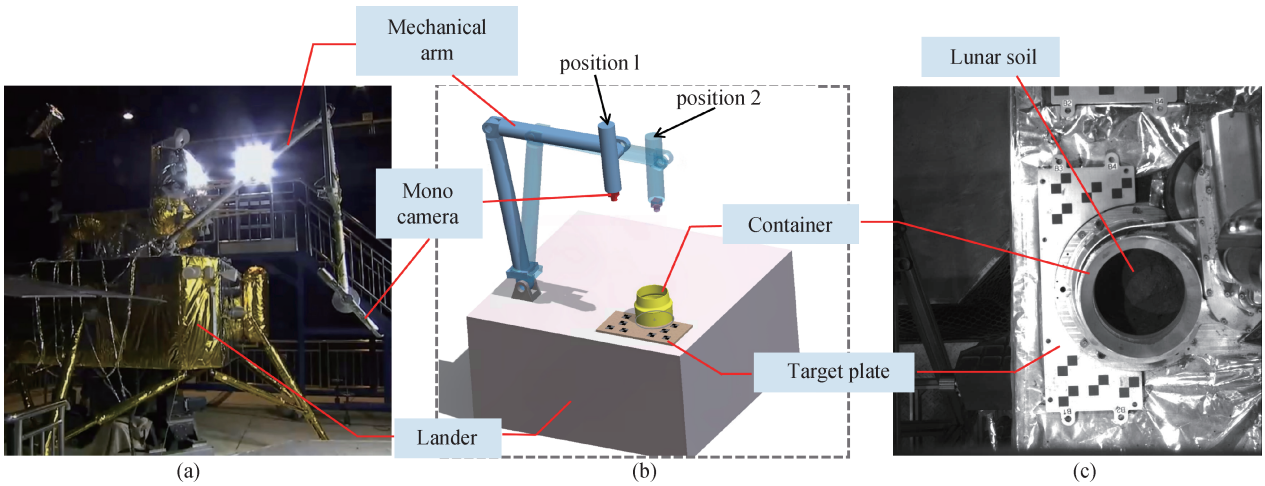


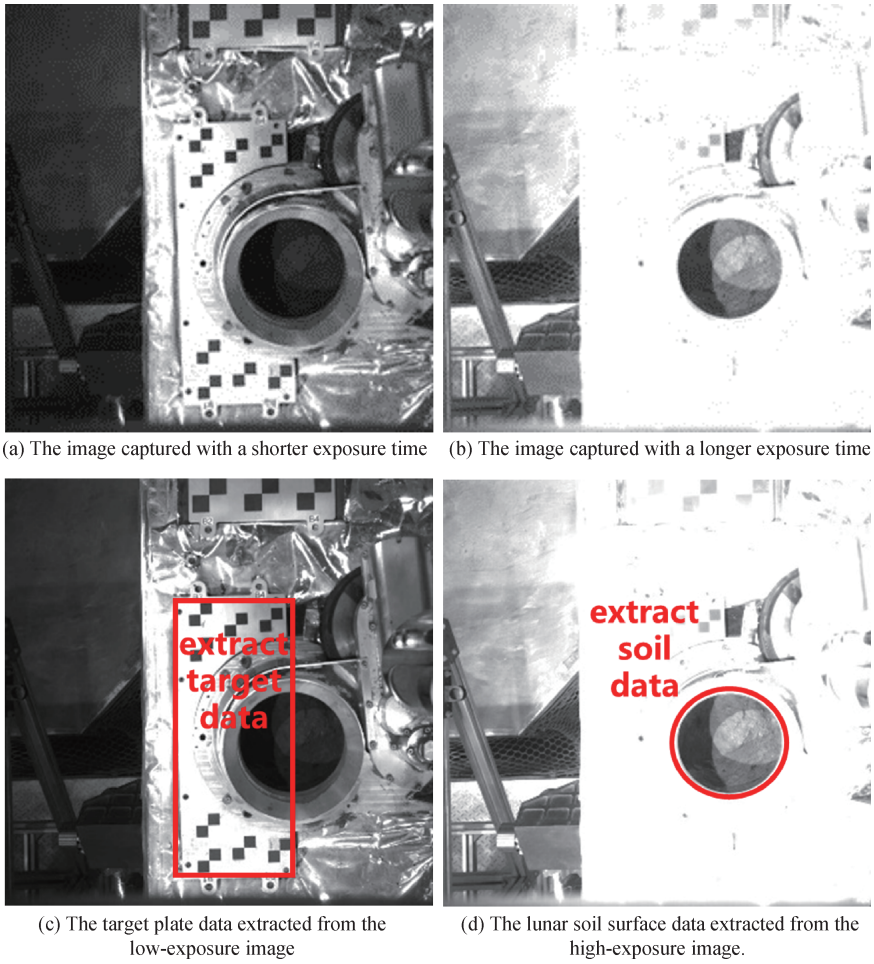
Fig.2 The system for image acquisition. (a) The lunar simulation environment with equipment identical to that of the Chang'E-6 lander. (b) A simplified model of the image acquisition hardware. (c) An example image captured by the camera.

Because of the demanding schedule, minimizing the number of image captures is essential. Consequently, images are captured at only two distinct positions.

The proposed algorithm utilizes the target plate information in the region directly illuminated by light to compute the camera pose. In addition, the algorithm uses the lunar soil information from the areas with weaker illumination in the image to reconstruct the lunar soil surface in the container. As depicted in Fig. 3, due to the significant difference in illumination between different

regions of the image, it is difficult to simultaneously utilize both the target plate information and the lunar soil surface information from a single image.

As Fig. 3 (a) shows, when the exposure time is short, the target plate information is relatively complete, but the section of lunar soil surface in the image lacks sufficient texture. Conversely, as shown in Fig. 3 (b), increasing the exposure time can enhance the texture details of the lunar soil surface in the image, but it may simultaneously result in overexposure of the target plate, leading to the loss of target information.



(a) The image captured with a shorter exposure time (b) The image captured with a longer exposure time

(c) The target plate data extracted from the low-exposure image (d) The lunar soil surface data extracted from the high-exposure image.

Fig.3 Images captured with different exposure times. (a) The image captured with a shorter exposure time. (b) The image captured with a longer exposure time. (c) The target plate data extracted from the low-exposure image. (d) The lunar soil surface data extracted from the high-exposure image.

We address this issue by capturing multiple images with different exposure times. As shown in Fig. 3(c) and Fig. 3(d), images with shorter exposure time are used to extract the target plate information, while images with longer exposure time are used to extract the lunar soil surface details.

Our final image acquisition plan is to capture images with different exposure times at two distinct locations, which will serve as the left and right images in a stereo system. The images with varying exposure times are used to extract target plate information and lunar soil surface information from regions with different illumination intensities in the camera's field of view.

3 Measurement Algorithm

Based on the images collected by the Chang'E-6 hardware system, we present a complete method for measuring the volume of lunar soil. The workflow is illustrated in Fig. 4 and consists of three modules: (1) camera pose estimation, (2) 3D reconstruction and point cloud extraction of lunar soil, and (3) volume calculation based on the point cloud.

3.1 Camera pose Estimation

The robotic arm of Chang'E-6 exhibits non-negligible deformation, so the pose of the camera mounted at the end of the arm cannot be obtained directly. Instead, the camera pose at the two positions is computed with the PnP (Perspective-n-Point) algorithm[37]. As shown in Fig. 2(c), eight targets with precisely measured 3D coordinates are distributed on the target plate surrounding the container. These eight target points serve as the feature points for the PnP algorithm,

and a dedicated extraction algorithm was designed for them.

In the Chang'E-6 mission, the camera's viewing angle and its distance to the sampling container vary only slightly, so the size and shape of the targets are similar in all captured images. We therefore use a multi-target template matching method to extract the 2D coordinates (u_i, v_i), $i = 1, 2, \ldots, 8$, of the eight target points.

The positions of the eight target points are expressed as follows:

$$\{(u_i, v_i) \mid (u_i, v_i) = \operatorname{argmax}\left(\operatorname{Coor}[x, y]\right), \\ \mid |x - u_0| \mid < R_1, \mid |y - v_0| \mid < R_2\} \tag{1}$$

where $\operatorname{Coor}[x, y]$ is the correlation coefficient between the template image and the captured image at pixel coordinate (x, y). The correlation matrix CorrMat is constructed by computing $\operatorname{Coor}[x, y]$ for all pixel positions within the search window; R_1 and R_2 define the half-size of the local search range around each target point, so the algorithm searches for extrema within a rectangular region of size $(2R_1 + 1) \times (2R_2 + 1)$ centered at each expected target location. The eight target points correspond to the eight local extrema (one global maximum and seven local maxima) of the correlation matrix. As shown in Algorithm 1, these eight extrema are detected by first finding the global maximum, then setting its surrounding region to zero to suppress it, and repeating this process until all remaining target points are found.

Because template matching produces high correlation both at the exact match location and at neighboring points, a fixed threshold or a simple global-maximum search would also extract the points surrounding each target. To address this problem of multi-target template detection, the integer coordinates of the targets are extracted as follows (Algorithm 1): the global maximum is first identified as a target point, its surrounding values in the correlation matrix are then set to zero to avoid false detections, and this process is repeated until all eight target points are detected.

Algorithm 1. Extraction of the 2D target coordinates

Input: correlation matrix CorrMat$[m][n]$, local search range $[R_1, R_2]$

Output: set of target pixel coordinate A

1:**function** MAIN()

2:$N \leftarrow 8$

3:$A \leftarrow \varnothing$

4:**for** $i \leftarrow 0$ **to** $N - 1$ **do**

5:search for the maximum value CorrMat$[j_i][k_i]$

6:$A \leftarrow A \cup \{(j_i, k_i)\}$

7:CorrMat$[j_i - R_1 : j_i + R_1][k_i - R_2 : k_i + R_2] \leftarrow 0$

8:**end for**

9:**end function**

The relationship between 2D pixel coordinates and 3D world coordinates can be shown as follows:

$$C_i = K_{\text{intri}}[R_{w \to c} | t_{w \to c}] C_w \tag{2}$$

where $C_w = [x_w, y_w, z_w, 1]^T$ is the location of a 3D point in the world coordinate system; $C_i = [u_i, v_i, 1]^T$ represents the homogeneous pixel coordinates of the corresponding 2D point; K_{intri} is the intrinsic matrix of the camera, calibrated on the ground. $R_{w \to c}$ and $t_{w \to c}$ are the rotation matrix and translation vector between the world and camera coordinate systems, which represent the camera poses to be solved. After obtaining the 2D and 3D coordinates of the targets, the camera poses $[R^{\text{left}}_{w \to c} | t^{\text{left}}_{w \to c}]$

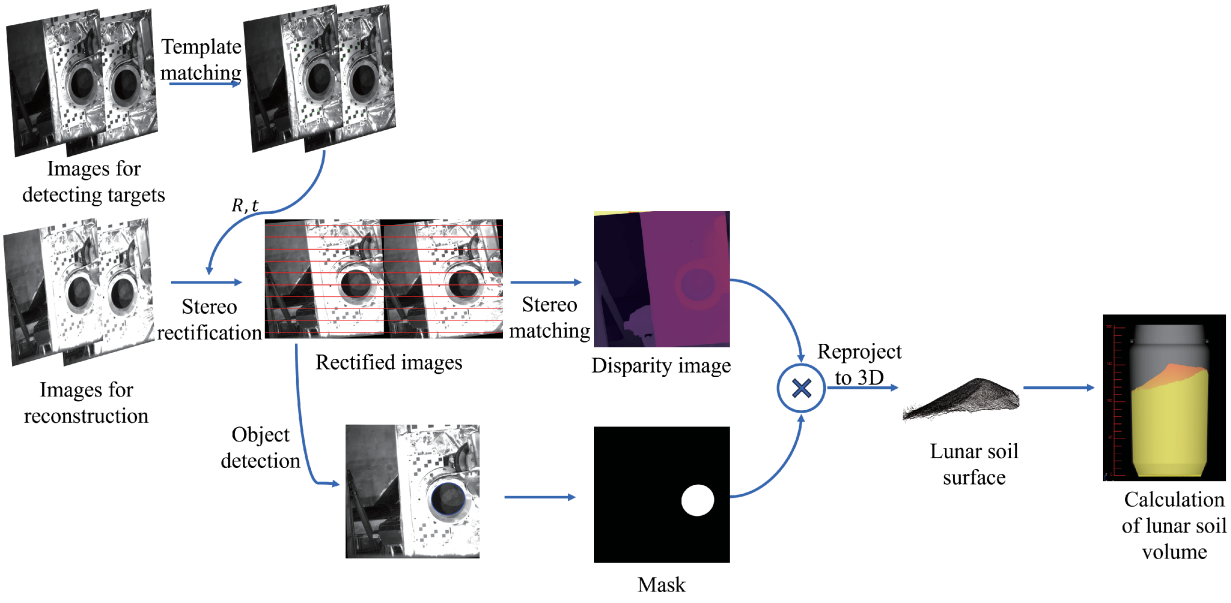


Fig.4 The workflow of the proposed method.

and $\left[R_{w\to c}^{\text{right}}|t_{w\to c}^{\text{right}}\right]$ at the two positions are obtained with the PnP algorithm[37,38]. The relative pose $[R|t]$ between camera position 1 and camera position 2 is then obtained as follows:

$$R = R_{w\to c}^{\text{right}} \times \left(R_{w\to c}^{\text{left}}\right)^{-1} \tag{3}$$

$$t = t_{w\to c}^{\text{right}} - R_{w\to c}^{\text{right}} \times \left(R_{w\to c}^{\text{left}}\right)^{-1} \times t_{w\to c}^{\text{left}} \tag{4}$$

3.2 Dense 3D Reconstruction and Object Point Cloud Extraction

Using the Bouguet stereo rectification algorithm[39], the images are corrected with the intrinsic matrix K_{intri} and the relative pose $[R|t]$. The stereo disparity is then inferred with CREStereo[19], which performs well in stereo matching.

The point cloud of the complete 3D scene is obtained from the stereo disparity. For the subsequent volume measurement, the point cloud corresponding to the upper surface of the lunar soil must be extracted. Based on the characteristics of stereo matching, this target point cloud is extracted by detecting the corresponding 2D image region. This approach avoids the more complex process of 3D point cloud extraction, reducing the algorithmic complexity.

As shown in Fig. 5(a), each pixel's disparity in the left image can be projected and mapped to a point $[x_w, y_w, z_w]^T$ in the 3D point cloud according to the stereo 3D reconstruction model. The mathematical expression of this correspondence is given as follows:

$$^T = \left[\frac{X}{W}\ \frac{Y}{W}\ \frac{Z}{W}\right]^T \tag{5}$$

$$\begin{bmatrix} X \\ Y \\ Z \\ W \end{bmatrix} = Q \begin{bmatrix} u \\ v \\ \text{disp} \\ 1 \end{bmatrix} \tag{6}$$

where $[u, v]$ is the pixel coordinate and disp is the disparity; Q is the projection matrix which is obtained by stereo rectification[39].

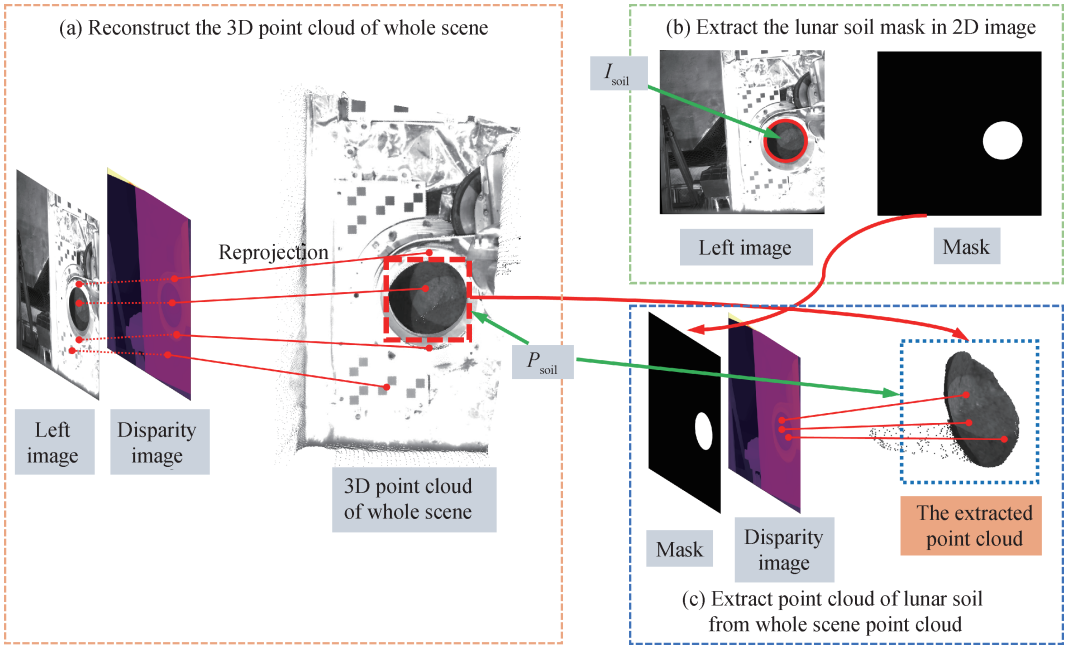


Fig.5 The extraction of the 3D point cloud of the lunar soil. (a) Reconstruction of the 3D point cloud of the complete scene. (b) Extraction of the mask corresponding to the lunar soil in the 2D image. (c) Generation of the lunar soil point cloud by reprojecting only the disparity within the mask region to 3D points.

As shown in Fig. 5(b), we first detect the image region $I_{\text{soil}} = \{(u_i, v_i)\}$ corresponding to the upper surface of the lunar soil in the rectified left image. Then, as shown in Fig. 5(c), when projecting the disparity to 3D coordinates with the projection matrix Q, only the disparity values within I_{soil} are projected into the 3D point cloud. The extracted point cloud P_{soil} is expressed as follows:

$$P_{\text{soil}} = \{c_w \,|\, c_w = Q[c_i, \text{disp}_i, 1]^T,\ c_i \in I_{\text{soil}}\} \tag{7}$$

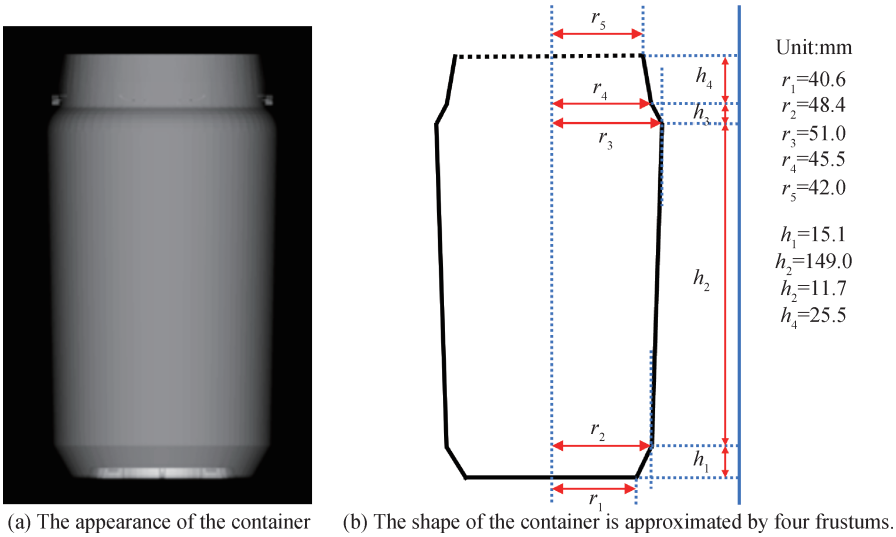
where P_{soil} is the point cloud of the upper surface of the lunar soil inside the sampling container.

3.3 Volume calculation based on point cloud data

The volume of lunar soil equals the space enclosed by the point cloud of the lunar soil surface and the container, which we therefore compute.

The container used to hold lunar soil in the Chang'E-6 mission is shown in Fig. 6. It is not a standard cylinder: its cross-section radius varies with height. Its shape can be approximated by four frustums, labeled Frum_1 to Frum_4 from bottom to top.

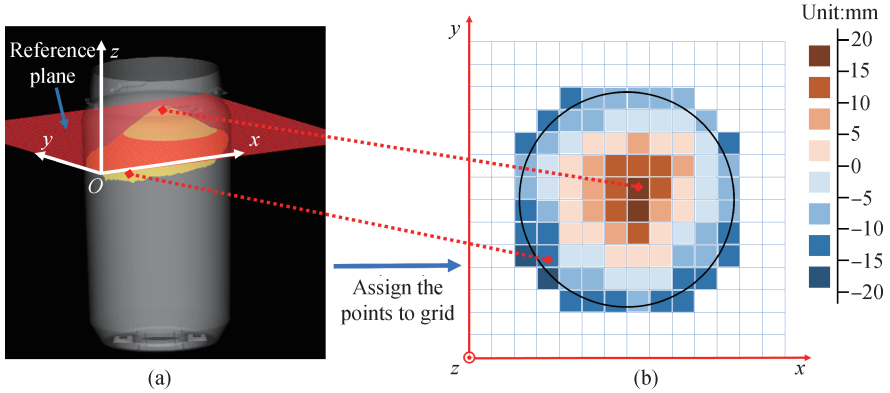
Calculating the volume of the lunar soil surface point cloud directly relative to the container bottom



(a) The appearance of the container (b) The shape of the container is approximated by four frustums.

Fig.6 The container. (a) The appearance of the container. (b) The shape of the container is approximated by four frustums.

with the grid method introduces significant error. As shown in Fig. 7(b), isolated points may also appear in the reconstructed point cloud because of stereo matching errors, further degrading the volume estimate. To reduce this error, we propose a more accurate method based on a reference plane, shown in Fig. 8. Instead of computing the volume directly relative to the container bottom, the average height of all points is first taken as the reference plane height ($h_{\text{ref}}=h_{\text{mean}}$). By splitting the calculation at this reference plane, isolated outliers below or far above the main soil surface have little impact on the final volume, because they are either excluded or averaged into the reference plane estimate.



(a) (b)

Fig.7 The calculation of volume V_{relative} between the upper surface of the lunar soil and the reference plane using the grid method. (a) Schematic diagram of the reference plane, coordinate system, the upper surface of the reconstructed lunar soil, and the container. (b) Points are assigned to the corresponding grids based on their x and y coordinates. We use different colors to roughly represent the average height of the point cloud within each grid relative to the height of the reference plane, i.e. $h_{\text{relative}}(x_i,y_i)$. It can be seen that the edge of the upper surface of the lunar soil is below the reference plane, so the corresponding relative height is negative.

First, the average height h_{mean} of all points in the extracted point cloud is computed, and the plane at this height is used as the reference plane, i. e., $h_{\text{ref}}=h_{\text{mean}}$. Based on this reference plane, the lunar soil is divided into two parts: the soil below the reference plane, V_{bel}, and the soil between the reference plane and the reconstructed surface, V_{relative}.

The soil below the reference plane is approximated as a set of conical frustums. As illustrated in Fig. 6(b), the container consists of four frustums (Frum$_1$ to Frum$_4$), and Fig. 9 shows the container structure and the reference plane. The volume below the reference plane is obtained by summing the volumes of the frustum segments intersected by the reference plane, as follows.

$$V_{\text{bel}}=\begin{cases} V_{\text{frum}}(r_1,r_{\text{n1}},h_{\text{n1}}), & 0<h_{\text{ref}}<h_1 \\ V_1+V_{\text{frum}}(r_2,r_{\text{n2}},h_{\text{n2}}), & h_1<h_{\text{ref}}<h_2 \\ V_1+V_2+V_{\text{frum}}(r_3,r_{\text{n3}},h_{\text{n3}}), & h_2<h_{\text{ref}}<h_3 \\ V_1+V_2+V_3+V_{\text{frum}}(r_4,r_{\text{n4}},h_{\text{n4}}), & h_3<h_{\text{ref}}<h_4 \end{cases} \tag{8}$$

$$V_{\text{frum}}(r_1,r_2,h)=\frac{1}{3}\pi h\left(r_1^2+r_2^2+r_1r_2\right) \tag{9}$$

where V_1, V_2, and V_3 are the volumes of Frum$_1$, Frum$_2$, and Frum$_3$, respectively, and r_{n1}, r_{n2}, r_{n3}, and r_{n4} denote the radii of the cross-sections at the reference plane height within each frustum. The intermediate variables

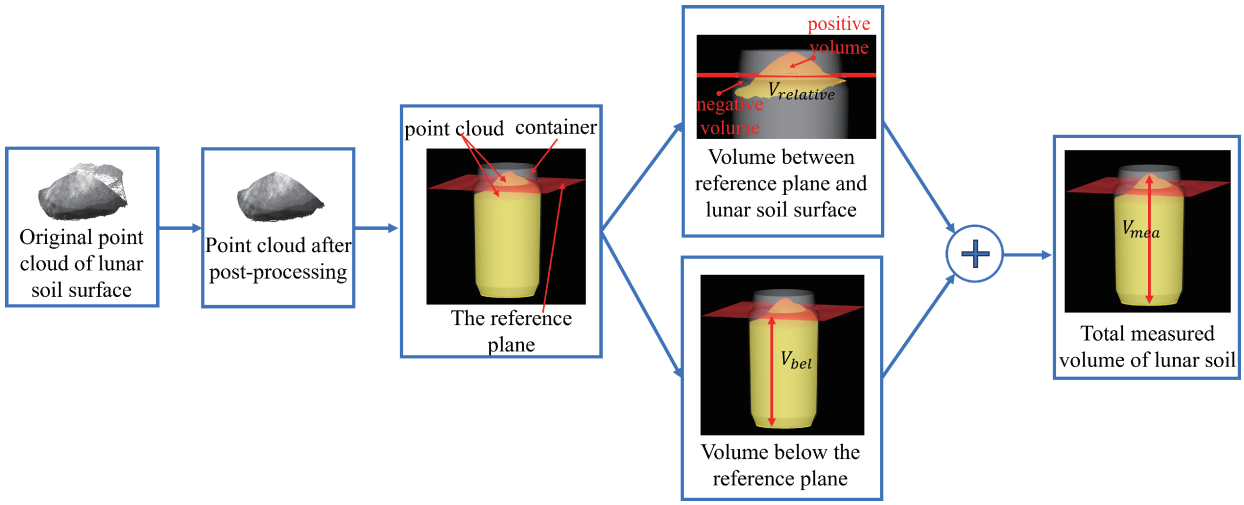


Fig.8 The volume calculation flowchart using the lunar soil point cloud. V_{relative} is the volume between the point cloud and the reference plane. V_{bel} represents the volume of the enclosed body formed by the reference plane and the container. The total measured volume V_{mea} is the sum of V_{relative} and V_{bel}.

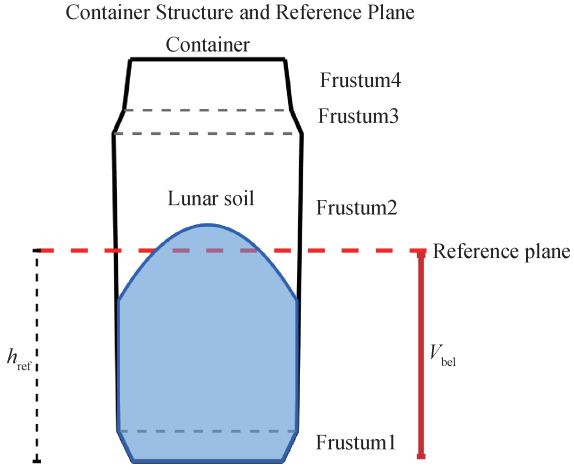


Fig.9 Schematic diagram of the container structure and the reference plane.

are defined as follows:

$$V_1 = V_{\text{frum}}(r_1, r_2, h_1),\ V_2 = V_{\text{frum}}(r_2, r_3, h_2),$$
$$V_3 = V_{\text{frum}}(r_3, r_4, h_3),\ h_{\text{n1}} = h_{\text{ref}},\ h_{\text{n2}} = h_{\text{ref}} - h_1,$$
$$h_{\text{n3}} = h_{\text{ref}} - h_1 - h_2,\ h_{\text{n4}} = h_{\text{ref}} - h_1 - h_2 - h_3,$$
$$r_{\text{n1}} = \frac{h_{\text{n1}}}{h_1}(r_2 - r_1) + r_1,\ r_{\text{n2}} = \frac{h_{\text{n2}}}{h_2}(r_3 - r_2) + r_2,$$
$$r_{\text{n3}} = \frac{h_{\text{n3}}}{h_3}(r_4 - r_3) + r_3,\ r_{\text{n4}} = \frac{h_{\text{n4}}}{h_4}(r_5 - r_4) + r_4.$$

The volume V_{relative} between the lunar soil surface and the reference plane is computed with the grid method. As shown in Fig. 7(a), a coordinate system is first established on the reference plane, with the XOY plane coinciding with it. Second, the cross-section of the container at the reference plane is divided into equally spaced grids. Only a few grids are drawn schematically in Fig. 7(b); in the actual calculation, the grid size is set to 1 mm, which yields many smaller grids. All points in the point cloud are then assigned to the corresponding grids according to their x and y coordinates. In Fig. 7(b), different colors roughly represent the average height of the points in each grid relative to the reference plane. The height within each grid relative to the reference plane is calculated as follows:

$$h_{\text{relative}}(x_i, y_i) = h_{\text{mean}}(x_i, y_i) - h_{\text{ref}} \tag{10}$$

where h_{ref} is the height of the reference plane, (x_i, y_i) denotes the position of a grid, and $h_{\text{mean}}(x_i, y_i)$ is the mean height of all 3D points assigned to grid (x_i, y_i). The middle part in Fig. 7(b) corresponds to the portion of the lunar soil surface above the reference plane in Fig. 7(a), so its relative height is positive. The edge part corresponds to the portion below the reference plane, so its relative height is negative. Finally, the volume of the surface relative to the reference plane is obtained by summing the equivalent volume of each grid. The volume V_{relative} is expressed as follows:

$$\begin{aligned} V_{\text{relative}} &= S_g^2 \times \sum_{i=1}^{n}\sum_{j=1}^{m}\left(h_{\text{relative}}(x_i, y_i)\right) \\ &= S_g^2 \times \sum_{i=1}^{n}\sum_{j=1}^{m}\left(h_{\text{mean}}(x_i, y_i) - h_{\text{ref}}\right) \end{aligned} \tag{11}$$

where $S_g = 1$ mm is the grid size, $h_{\text{mean}}(x_i, y_i)$ is the mean height of the points in grid (x_i, y_i), and h_{ref} is the height of the reference plane.

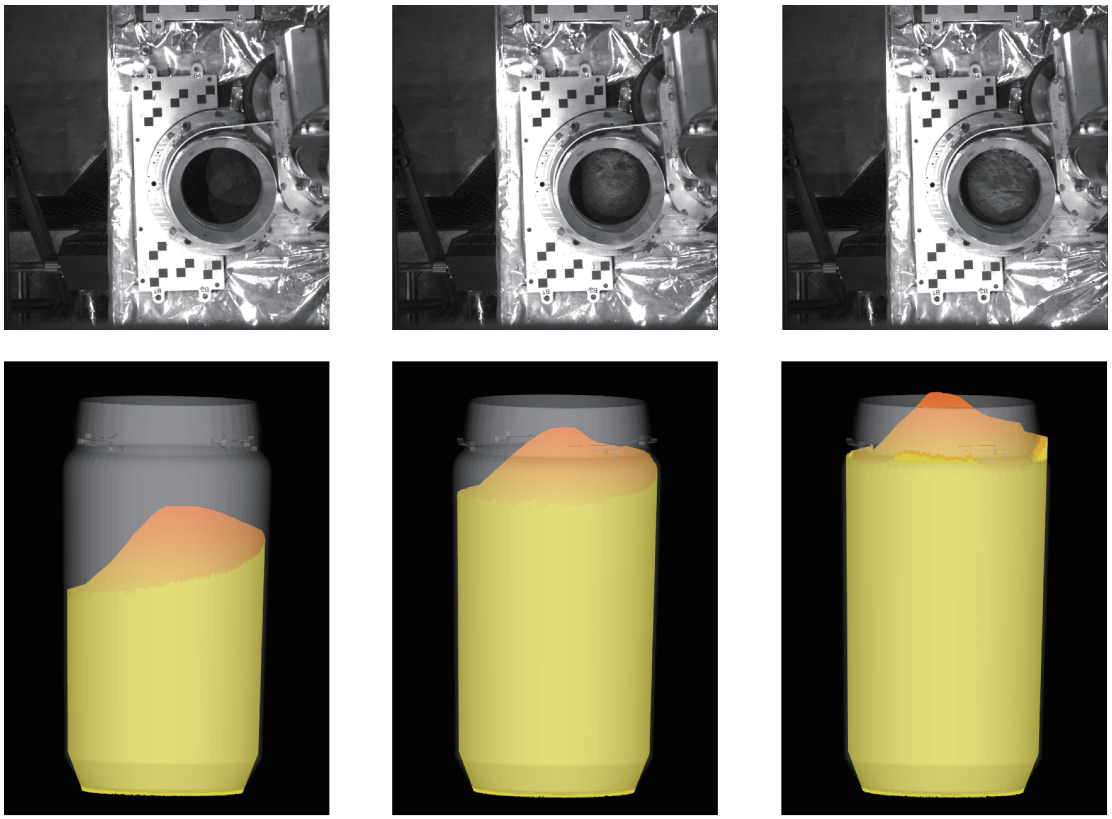
The final measured volume of lunar soil in the container is obtained as follows:

$$V_{\text{mea}} = V_{\text{bel}} + V_{\text{relative}} \tag{12}$$

4 Experiments and results

The proposed algorithm was tested in both the lunar simulation environment on Earth and the actual lunar environment during the Chang'E-6 mission. Twelve experiments were conducted in the simulation environment, and the results are presented in Table 1, where V_{mea} denotes the volume measured by the proposed method. The actual volume V_{act} was obtained by pouring

each sample into a precision graduated cylinder and reading the settled volume directly from its scale. The cylinder is a Class A precision graduated cylinder conforming to ISO 4788, and its calibration is traceable to the national capacity standard. Its capacity is 1000 cm^3 with a capacity tolerance of ±5 cm^3; sample volumes exceeding this capacity were obtained by summing two successive readings. Evaluated through repeated water filling and reading, the reading repeatability of the cylinder is within ±2 cm^3. Some results are shown in Fig. 10.



(a) Measured volume: 975 cm^3
Actual volume: 970 cm^3

(b) Measured volume: 1 309 cm^3
Actual volume: 1 320 cm^3

(c) Measured volume: 1 405 cm^3
Actual volume: 1 395 cm^3

Fig.10 Experimental results of lunar soil volume measurement: the upper row shows the images captured at one position, and the lower row shows the point cloud of the lunar soil. We compared the measured volume using our method with the actual volume.

The twelve ground tests showed that the proposed method measured the lunar soil volume accurately, with an absolute error of at most 17 cm^3 (Fig. 11). The mean absolute error (MAE), the root mean square error (RMSE), and the relative error were also computed from the twelve experiments; the MAE and RMSE were 9.3 cm^3 and 11.0 cm^3, respectively, and the per-experiment relative errors are listed in Table 1. The relative error is larger at small volumes and decreases as the container approaches full: it reached 5.0% and 8.5% at 140 cm^3 and 200 cm^3, respectively, while near full it

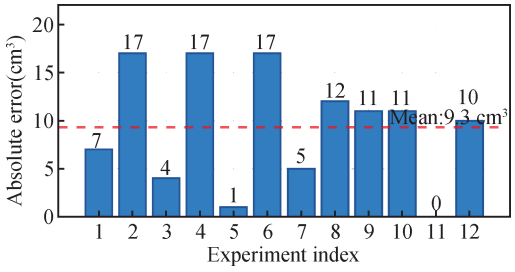


Fig.11 Absolute error of volume measurement for the twelve experiments.

Table 1 Experimental results in the lunar simulation environment on Earth.

No.	h_{ref} (mm)	V_{mea} (cm^3)	V_{act} (cm^3)	Abs. Error (cm^3)	Rel. Error (%)
1	22.5	133	140	7	5.0
2	29.3	183	200	17	8.5
3	52.1	361	365	4	1.1
4	84.8	602	585	17	2.9
5	101.9	749	750	1	0.1
6	130.6	957	940	17	1.8
7	132.5	975	970	5	0.5
8	151.9	1122	1110	12	1.1
9	155.5	1156	1145	11	1.0
10	175.3	1309	1320	11	0.8
11	182.1	1355	1355	0	0.0
12	190.1	1405	1395	10	0.7

stayed below 1%. This trend follows from the filling height and the effective reconstruction area. At low filling heights, the reference plane is low, the reconstructed soil surface is small, and the boundary region, where disparity estimates are least reliable, accounts for a larger fraction of the surface, so the bounded absolute error (at most 17 cm^3) produces a larger relative error. As the fill height rises, the reference plane moves up and the effective reconstruction area grows, so the same bounded absolute error yields a much smaller relative error. The method therefore maintains stable absolute accuracy over the whole volume range, with relative accuracy improving as the container approaches full.

The main uncertainty sources of the measurement system are: (1) camera intrinsic calibration; (2) the three-dimensional coordinates and image localization of the targets; (3) PnP-based pose estimation; (4) stereo disparity estimation; (5) the geometric parameters of the container; and (6) numerical volume integration. The intrinsic calibration error propagates through stereo rectification and the projection matrix Q into the reconstructed point coordinates. Errors in the target coordinates and their image localization propagate into the camera pose and, in turn, the stereo reconstruction. Disparity estimation is a major source of surface uncertainty, particularly in low-texture regions and near the container boundary. The container geometry affects the volume below the reference plane V_{bel}, and the grid-based integration introduces a discretization error in V_{relative}. These sources together limit the achievable accuracy and account for the observed absolute errors.

To assess the contribution of the reference-plane strategy, the proposed mean-height reference plane was compared with four alternatives on the same twelve datasets: (1) direct integration without a reference plane, which integrates the point cloud down to the container bottom; (2) a median-based reference height; (3) a trimmed-mean reference height; and (4) robust plane fitting. The MAE and RMSE of each strategy are listed in Table 2. The mean-height reference plane gave the lowest MAE (9.3 cm^3) and RMSE (11.0 cm^3), close to those of the median and trimmed-mean heights, which confirmed the mean as a reasonable and stable reference height. Direct integration was much worse because its point cloud loses part of the boundary and distorts the surface relief: the viewing angle and the container opening occlude part of the inner boundary, and the stereo matching error further corrupts the reconstructed surface. Integrated down to the container bottom, the missing boundary produces a systematic underestimation, and the distorted relief propagates into the volume. The reference-plane strategy avoided this by splitting the volume into V_{bel}, computed from the known container geometry and therefore insensitive to boundary loss, and V_{relative}, which captures only the surface relief relative to the reference plane; the boundary loss and distortion were thus confined to the small V_{relative} term. Robust plane fitting was also less accurate because the soil surface is not planar, so a single fitted plane cannot follow the relief and its tilt amplifies the error near the boundary. The comparison confirmed that the reference-plane decomposition is the main contributor to the accuracy and stability of the volume estimate.

Table 2 Comparison of the proposed volume calculation strategy with representative alternatives on the twelve experiments.

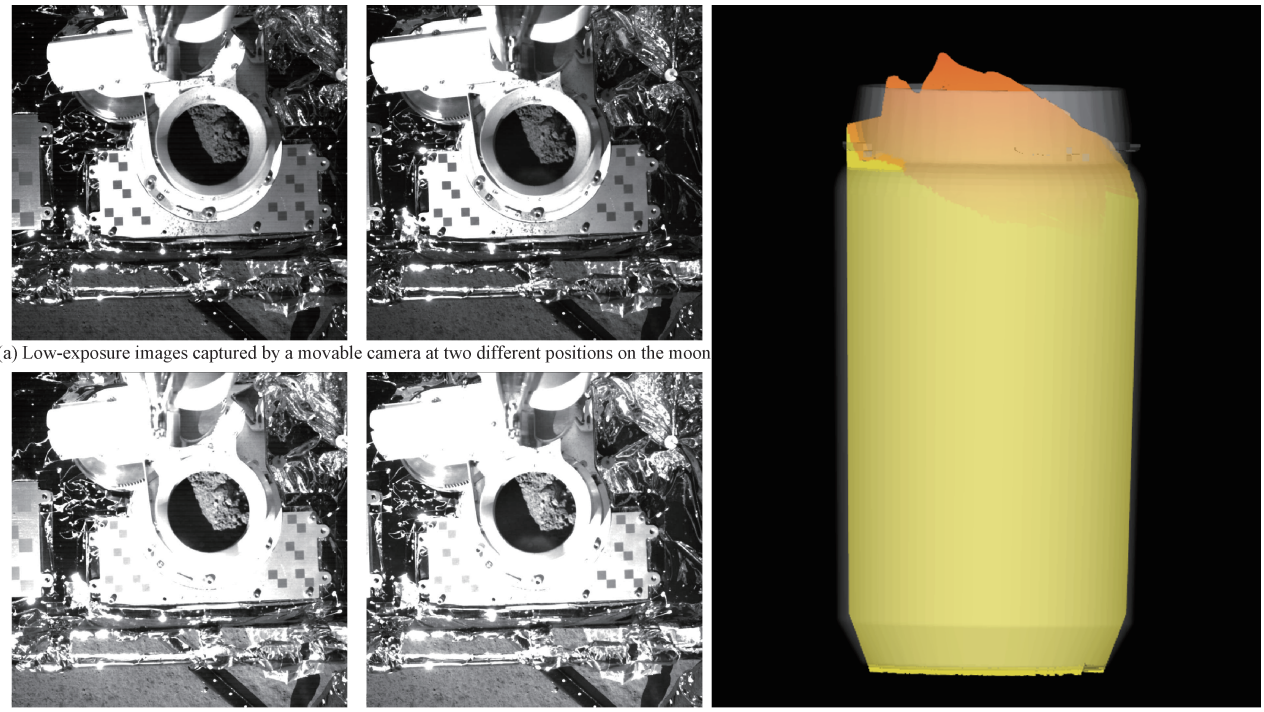
Strategy	MAE(cm^3)	RMSE(cm^3)
Direct integration (no reference plane)	35.6	43.8
Robust plane fitting	16.4	20.7
Median reference height	9.9	11.6
Trimmed-mean reference height	9.7	11.4
Proposed mean reference height	9.3	11.0

In addition to the tests in the lunar simulation environment, the proposed method was also used during the Chang'E-6 mission. On June 3, 2024, during lunar soil collection on the farside of the Moon, Chang'E-6 used the proposed algorithm to measure the volume of lunar soil inside the container.

Fig. 12(a) shows the low-exposure images captured by Chang'E-6 on the Moon from two different positions with the movable camera, used to extract the pixel coordinates of the target points. Fig. 12(b) shows the high-exposure images used to reconstruct the point cloud of the lunar soil surface, and Fig. 12(c) shows the reconstructed point cloud of the lunar soil in the container. The measured volume of lunar soil was 1393 cm^3. Based on this result, the Chang'E-6 team determined that the container was nearly full and that the amount of lunar soil had reached the expected target, so they decided to stop scooping after eight scoops.

5 Conclusion

In this paper, we proposed a complete method for measuring the volume of lunar soil in the Chang'E-6 sampling container, comprising an image acquisition scheme and a volume measurement algorithm. A single camera was moved to two positions to form a stereo image pair, and images with different exposure times were captured to extract the target information and the lunar soil surface separately. Since the camera pose cannot be obtained directly, a PnP-based method was used to estimate it. A simplified point cloud extraction method based on the correspondence between disparity maps and the point cloud avoided complex 3D point cloud extraction, and the soil volume was computed from the space enclosed by the point cloud and the container. Ground simulation experiments showed that the proposed method measured the soil volume accurately, with an absolute error of at most 17 cm^3. During the Chang'E-6



(a) Low-exposure images captured by a movable camera at two different positions on the moon

(b) High-exposure images captured at the same two positions after adjusting the exposure settings

(c) The reconstructed point cloud of the lunar soil

Fig.12 Images captured by Chang'E-6 on the farside of the Moon and the results of lunar soil volume measurement. (a) Low-exposure images captured by a movable camera at two different positions on the Moon. (b) High-exposure images captured at the same two positions after adjusting the exposure settings. (c) The reconstructed point cloud of the lunar soil; the measured volume is 1393 cm^3.

mission, the method measured the lunar soil volume as 1393 cm^3, which assisted the team in confirming that the sampling target had been reached and that it was the optimal time to stop scooping.

Future work could address camera pose estimation and stereo matching. For pose estimation and stereo rectification, one alternative is to match feature points between the two images and then recover the scale from the known 3D coordinates of the eight target points. In addition, because the lunar soil surface has weak texture and many repetitive structures, a dedicated module could be designed to optimize stereo matching based on these characteristics.

Author Contribution:

Conceptualization, J. L., M. Y. and Y. Q.; Methodology, J. L., M. Y. and Y. Z.; Software, M. Y.; Validation, M.Y., Y.Z., and L.M.; Formal analysis, M.Y.; Investigation, M.Y., Y.Z., and L.M.; Data curation, M.Y. and L.M.; Writing—original draft preparation, J.L. and M. Y.; Writing—review and editing, J.L., M.Y., X.D., and Y. Q.; Visualization, M. Y.; Supervision, X. D. and Y. Q.; Project administration, X. D. and Y. Q.; Funding acquisition, X. D. and Y. Q. All authors have read and agreed to the published version of the manuscript.

Acknowledgments:

The authors would like to thank the Chang'E-6 mission team of China Academy of Space Technology for their support and collaboration.

Funding Information:

This work was supported by the China Academy of Space Technology and the Chang'E-6 mission of China. No specific grant or project number was assigned to this funding.

Data Availability:

The data supporting the findings of this study are available within the paper. Additional data are not publicly available due to privacy and mission-related restrictions.

Conflict of Interest:

The authors declare no competing interests.

Ethics Statement:

Not applicable.

Use of Generative AI and AI-Assisted Technologies:

During the preparation of this manuscript, the authors used DeepSeek-V4-Pro to assist with grammar checking, language polishing, and formatting. No generative AI was used to generate research content, data, figures, or analysis. The authors reviewed and edited all content and take full responsibility for the manuscript.

References

[1] T. Zhang, B. Wang, H. Wei, Y. Zhang, C. Chao, K. Xu, X. Ding, X. Hou, and Z. Zhao, "Review on planetary regolith-

sampling technology," *Progress in Aerospace Sciences* , vol. 127, p. 100760, **2021**, doi: 10.1016/j.paerosci.2021.100760.

[2] S. T. Arzo, D. Sikeridis, M. Devetsikiotis, F. Granelli, R. Fierro, M. Esmaeili, and Z. Akhavan, "Essential technologies and concepts for massive space exploration: Challenges and opportunities, " *IEEE Transactions on Aerospace and Electronic Systems* , vol. 59, no. 1, pp. 3-29, **2022**, doi: 10.1109/TAES.2022.3169126.

[3] S. Hu, H. He, J. Ji, Y. Lin, H. Hui, M. Anand, R. Tartèse, Y. Yan, J. Hao, R. Li, L. Gu, Q. Guo, H. He, and Z. Ouyang, "A dry lunar mantle reservoir for young mare basalts of Chang'E-5," *Nature* , vol. 600, no. 7887, pp. 49-53, **2021**, doi: 10.1038/s41586-021-04107-9.

[4] W. Yang and Y. Lin, "New lunar samples returned by Chang'E-5: Opportunities for new discoveries and international collaboration, " The Innovation, vol. 2, no. 1, 2021, doi: 10.1016/j.xinn.**2020**.100070.

[5] Y. Chen, S. Hu, J.-H. Li, Q.-L. Li, X. Li, Y. Li, Y. Liu, Y. Qian, W. Yang, Q. Zhou, Y. Lin, C. Li, and X. -H. Li, "Chang'E-5 lunar samples shed new light on the Moon," *The Innovation Geoscience* , vol. 1, no. 1, pp. 100014-1, 2023, doi: 10.59717/j.xinn-geo.**2023**.100014.

[6] J. A. Wood, J. S. Dickey Jr., U. B. Marvin, and B. N. Powell, "Lunar anorthosites," Science, vol. 167, no. 3918, pp. 602-604, 1970, doi: 10.1126/science.167.3918.602.

[7] J. Smith, A. Anderson, R. Newton, E. Olsen, A. Crewe, M. Isaacson, D. Johnson, and P. Wyllie, "*Petrologic history of the Moon inferred from petrography* , mineralogy and petrogenesis of Apollo 11 rocks, " in *Proceedings of the Apollo* 11 lunar science conference, Pergamon Press, **1970**, p. 897.

[8] X. Che, A. Nemchin, D. Liu, T. Long, C. Wang, M. D. Norman, K. H. Joy, R. Tartèse, J. Head, B. Jolliff, J. F. Snape, C. R. Neal, M. J. Whitehouse, C. Crow, G. Benedix, F. Jourdan, Z. Yang, C. Yang, J. Liu, S. Xie, Z. Bao, R. Fan, D. Li, Z. Li, and S. G. Webb, "*Age and composition of young basalts on the Moon* , measured from samples returned by Chang'E-5," Science, vol. 374, no. 6569, pp. 887-890, **2021**, doi: 10.1126/science.abl7957.

[9] J. H. Allton, "Catalog of Apollo lunar surface geological sampling tools and containers," NASA Lyndon B. *Johnson Space Center* , 1989.

[10] L. Xiao, Y. Qian, Q. Wang, and Q. Wang, "The Chang'E-5 mission," in Sample return missions, Elsevier, **2021**, pp. 195-206. doi: 10.1016/B978-0-12-818330-4.00009-4.

[11] E. Slyuta, "The Luna program," *in Sample return missions* , Elsevier, **2021**, pp. 37-78. doi: 10.1016/B978-0-12-818330-4.00003-3.

[12] D. H. Le Croissette, "The scientific instruments on Surveyor," *IEEE Transactions on Aerospace and Electronic Systems* , vol. AES-5, no. 1, pp. 2-21, 1969, doi: 10.1109/TAES.1969.309815.

[13] L. Liu and C. Hu, "*Scheme design of the CHANG'E-5T* 1 extended mission," Chinese Journal of Aeronautics, vol. 31, no. 7, pp. 1559-1567, **2018**, doi: 10.1016/j.cja.2018.04.012.

[14] Y. Wang, J. Nan, C. Zhao, B. Xie, S. Gou, Z. Yue, K. Di, H. Zhang, X. Deng, and S. Sun, "A catalogue of impact craters and surface age analysis in the Chang'E-6 landing area, " *Remote Sensing* , vol. 16, no. 11, p. 2014, **2024**, doi: 10.3390/rs16112014.

[15] Z. Jia, J. Chen, J. Kong, L. Qiao, X. Fu, and Z. Ling, "Geologic context of Chang'E-6 candidate landing regions and potential non-mare materials in the returned samples, " *Icarus* , vol. 416, p. 116107, **2024**, doi: 10.1016/j.icarus.2024.116107.

[16] C. Zhou, Y. Jia, J. Liu, H. Li, Y. Fan, Z. Zhang, Y. Liu, Y. Jiang, B. Zhou, Z. He, J. Yang, Y. Hu, Z. Liu, L. Qin, B. Lv, Z. Fu, J. Yan, C. Wang, and Y. Zou, "Scientific objectives and payloads of the lunar sample return mission—Chang'E-5, " *Advances in Space Research* , vol. 69, no. 1, pp. 823-836, **2022**, doi: 10.1016/j.asr.2021.09.001.

[17] C. Chen, X. Jia, G. Zhang, Y. Zheng, X. Deng, and Y. Qu, "Vision-based sampling implementation in the Chang'E-6 lunar farside sample return mission, " *Light: Advanced Manufacturing* , vol. 6, no. 1, p. 10, **2025**, doi: 10.37188/lam.2025.010.

[18] L. Lipson, Z. Teed, and J. Deng, "RAFT-Stereo: Multilevel recurrent field transforms for stereo matching, " in *2021 international conference on 3D vision (3DV)* , IEEE, **2021**, pp. 218-227. doi: 10.1109/3DV53792.2021.00032.

[19] J. Li, P. Wang, P. Xiong, T. Cai, Z. Yan, L. Yang, J. Liu, H. Fan, and S. Liu, "Practical stereo matching via cascaded recurrent network with adaptive correlation," *in Proceedings of the IEEE/CVF conference on computer vision and pattern recognition* , **2022**, pp. 16263-16272. doi: 10.1109/CVPR52688.2022.01578.

[20] H. Zhao, H. Zhou, Y. Zhang, J. Chen, Y. Yang, and Y. Zhao, "High-frequency stereo matching network," *in Proceedings of the IEEE/CVF conference on computer vision and pattern recognition* , **2023**, pp. 1327-1336. doi: 10.1109/CVPR52729.2023.00134.

[21] B. Lin, F. Xing, L. Su, K. Wang, Y. Liu, D. Zhang, X. Yang, H. Tan, Z. Zhu, and D. Wang, "Real-time and universal network for volumetric imaging from microscale to macroscale at high resolution, " *Light: Science & Applications* , vol. 14, p. 178, **2025**, doi: 10.1038/s41377-025-01842-w.

[22] C. Zevallos-Delgado, T. T. Mekonnen, A. W. Schill, M. Singh, S. R. Aglyamov, and K. V. Larin, "Air-coupled ultrasound based noncontact reverberant optical coherence elastography," *Light: Advanced Manufacturing* , vol. 6, p. 76, 2025, doi: 10.37188/lam.**2025**.076.

[23] G. Coulouma, D. Feurer, F. Vinatier, and O. Huttel, "Assessing new sensor-based volume measurement methods for high-throughput bulk density estimation in the field under various soil conditions," *European Journal of Soil Science* , vol. 72, no. 5, pp. 2049-2061, **2021**, doi: 10.1111/ejss.13115.

[24] M. Acuna and A. Sosa, "*Automated volumetric measurements*

of truckloads through multi-view photogrammetry and **3**D reconstruction software, " *Croatian Journal of Forest Engineering:* Journal for Theory and Application of Forestry Engineering, vol. 40, no. 1, pp. 151-162, 2019.

[25] E. Heng Siong, M. F. M. Ariff, and A. F. Razali, "The application of smartphone based Structure from Motion (SfM) photogrammetry in ground volume measurement," *The International Archives of the Photogrammetry* , Remote Sensing and Spatial Information Sciences, vol. 48, pp. 145-152, **2023**, doi: 10.5194/isprs-archives-XLVIII-4-W6-2022-145-2023.

[26] H. Anwar, S. M. Abbas, A. Muhammad, and K. Berns, "*Volumetric estimation of contained soil using* **3**D sensors," in *Intl*. Commercial vehicle technology symposium, Citeseer, **2014**, pp. 11-13.

[27] R. Zhang, S. Lian, L. Li, L. Zhang, C. Zhang, and L. Chen, "Design and experiment of a binocular vision-based canopy volume extraction system for precision pesticide application by UAVs," *Computers and Electronics in Agriculture* , vol. 213, p. 108197, **2023**, doi: 10.1016/j.compag.2023.108197.

[28] A. Tabb and H. Medeiros, "A robotic vision system to measure tree traits, " in *2017 IEEE/RSJ international conference on intelligent robots and systems (IROS)* , IEEE, **2017**, pp. 6005-6012. doi: 10.1109/IROS.2017.8206497.

[29] Y. Zhu, S. Cao, T. Song, Z. Xu, and Q. Jiang, "**3**D reconstruction and volume measurement of irregular objects based on RGB-D camera, " Measurement Science and Technology, vol. 35, no. 12, p. 125010, **2024**, doi: 10.1088/1361-6501/ad7621.

[30] J. Kongsro, "Estimation of pig weight using a Microsoft Kinect prototype imaging system, " *Computers and Electronics in Agriculture* , vol. 109, pp. 32-35, **2014**, doi: 10.1016/j.compag.2014.08.008.

[31] A. Pezzuolo, M. Guarino, L. Sartori, L. A. González, and F. Marinello, "On-barn pig weight estimation based on body measurements by a Kinect v1 depth camera," *Computers and electronics in agriculture* , vol. 148, pp. 29-36, **2018**, doi: 10.1016/j.compag.2018.03.003.

[32] K. Mori, D. Kono, and A. Matsubara, "Vision-based volumetric displacement measurement with a self-illuminating target," *CIRP Annals* , vol. 72, no. 1, pp. 305-308, **2023**, doi: 10.1016/j.cirp.2023.04.059.

[33] M. Kamari and Y. Ham, "Vision-based volumetric measurements via deep learning-based point cloud segmentation for material management in jobsites, " *Automation in Construction* , vol. 121, p. 103430, **2021**, doi: 10.1016/j.autcon.2020.103430.

[34] J. Chen, W. Lu, L. Yuan, Y. Wu, and F. Xue, "Estimating construction waste truck payload volume using monocular vision," *Resources* , Conservation and Recycling, vol. 177, p. 106013, **2022**, doi: 10.1016/j.resconrec.2021.106013.

[35] Z. Zhao, V. Kravtsov, Z. Wang, Z. Zhou, L. Dou, D. Huang, Z. Wang, X. Cheng, M. B. Raschke, and T. Jiang, "Applications of ultrafast nano-spectroscopy and nano-imaging with tip-based microscopy," *eLight* , vol. 5, no. 1, p. 1, **2025**, doi: 10.1186/s43593-024-00079-1.

[36] X. Dun, J. Zhang, F. Chen, Z. Zhang, X. Wang, Y. Xing, S. Dong, Z. Fan, Y. Shi, G. Wetzstein, Z. Wang, and X. Cheng, "Neural array meta-imaging," *eLight* , vol. 5, p. 33, **2025**, doi: 10.1186/s43593-025-00107-8.

[37] V. Lepetit, F. Moreno-Noguer, and P. Fua, "EPnP: An Accurate O(n) Solution to the PnP Problem," *International journal of computer vision* , vol. 81, pp. 155-166, **2009**, doi: 10.1007/s11263-008-0152-6.

[38] C. Liu, W. Guo, W. Hu, R. Chen, and J. Liu, "*Real-time crater-based monocular* **3**-D pose tracking for planetary landing and navigation," IEEE Transactions on Aerospace and Electronic Systems, vol. 59, no. 1, pp. 311-335, **2022**, doi: 10.1109/TAES.2022.3184660.

[39] J.-Y. Bouguet, "Camera Calibration Toolbox for MATLAB." [Online]. *Available: http://www. vision. caltech. edu/bouguetj/calib_doc/* , **2004**.